PAPER • OPEN ACCESS

Third order nonlinear correlation of the electromagnetic vacuum at near-infrared frequencies

To cite this article: Francesca Fabiana Settembrini *et al* 2024 *New J. Phys.* **26** 043017

IOP Publishing New J. Phys. 26 (2024) 043017 https://doi.org/10.1088/1367-2630/ad3b32

New Journal of Physics
The open access journal at the forefront of physics

Deutsche Physikalische Gesellschaft DPG
IOP Institute of Physics

Published in partnership with: Deutsche Physikalische Gesellschaft and the Institute of Physics

OPEN ACCESS

RECEIVED
20 September 2023

REVISED
19 March 2024

ACCEPTED FOR PUBLICATION
5 April 2024

PUBLISHED
22 April 2024

PAPER

Third order nonlinear correlation of the electromagnetic vacuum at near-infrared frequencies

Francesca Fabiana Settembrini, Alexa Herter* and Jérôme Faist

ETH Zürich, Institute of Quantum Electronics, Auguste-Piccard-Hof 1, 8093 Zürich, Switzerland
* Author to whom any correspondence should be addressed.

E-mail: aherter@ethz.ch, fabiana.settembrini@point.cloud and jfaist@ethz.ch

Keywords: electro-optic sampling, third-order nonlinear effect, correlation of vacuum electric field

Supplementary material for this article is available online

Abstract

In recent years, electro-optic sampling, which is based on Pockel's effect between an electromagnetic mode and a copropagating, phase-matched ultrashort probe, has been largely used for the investigation of broadband quantum states of light, especially in the mid-infrared and terahertz frequency range. The use of two mutually delayed femtosecond pulses at near-infrared frequencies allows the measurement of quantum electromagnetic radiation in different space-time points. Their correlation allows therefore direct access to the spectral content of a broadband quantum state at terahertz frequencies after Fourier transformation. In this work, we will prove experimentally and theoretically that when using strongly focused coherent ultrashort probes, the electro-optic sampling technique can be affected by the presence of a third-order nonlinear mixing of the probes' electric field at near-infrared frequencies. Moreover, we will show that these third-order nonlinear phenomena can also influence correlation measurements of the quantum electromagnetic radiation. We will prove that the four-wave mixing of the coherent probes' electric field with their own electromagnetic vacuum at near-infrared frequencies results in the generation of a higher-order nonlinear correlation term. The latter will be characterized experimentally, proving its local nature requiring the physical overlap of the two probes. The parameters regime where higher order nonlinear correlation results predominant with respect to electro-optic correlation of terahertz radiation is provided.

1. Introduction

Nonlinear quantum optics [1] has been of paramount importance for recent technological developments in a multitude of research fields, from optical quantum communication [2], quantum computing [3] to quantum spectroscopy [4] and quantum metrology [5]. In particular, the optimization of nonlinear photon–photon interaction has been crucial for the implementation of new platforms for quantum logic integrated on-chip [6–8] and of building blocks for efficient entanglement and squeezed radiation generation, which is fundamental for improved performances in quantum sensing [9].

Nonlinear interaction of photons at different frequencies has been particularly significant for the metrological study of fundamental states of electromagnetic radiation, especially in the mid-infrared (MIR) and terahertz (THz) frequency range. In alternative to commonly used heterodyne detection, an established measurement scheme compatible with the investigation of the most fundamental broadband states of electromagnetic radiation has been developed through electro-optic sampling (EOS) [10]. This measurement technique exploits the Pockels effect in a material with $\chi^{(2)}$ nonlinearity to map the amplitude of the investigated electromagnetic field on the polarization state of a phase-matched femtosecond pulse. The use of ultrashort laser pulses insures the subcycle resolution of the electromagnetic radiation under study both in space and in time and the nonlinear properties of the material determine the large detection bandwidth of the technique.

Experimental implementations of electro-optic detection have led to the first measurements of the statistical properties of the electromagnetic vacuum in the MIR frequency range [11, 12], through a parametric study of the detection system's shot noise. These results have led to further theoretical proposals in the field of quantum metrology for the exploration of higher order noise distributions of the electromagnetic vacuum [13–16].

In previous works, we have presented a further development of the electro-optic field detection technique involving the use of two probing pulses, which enables the measurement of electromagnetic radiation in distinct space-time points. This opened up the possibility of investigating both second- [17] and first-order coherence on an electromagnetic quantum state of radiation, which provides access to its spectral content after a Fourier transformation. We have experimentally proven that the developed electro-optic field correlation measurement scheme allows access to the spatial and temporal coherence of the electromagnetic quantum vacuum in the THz frequency range [18]. In particular, our latest results [19] investigating field correlations with spatially separated beams have provided the first experimental proof of a fundamental hypothesis in quantum electrodynamics, which claims the quantum vacuum to be correlated outside the relativistic light cone [20].

In order to improve the accuracy of quantum metrology measurements based on electro-optic sampling, a strong confinement of the probing radiation in both space and time is needed. However, the presence of a strong local probing electric field will influence the measured electromagnetic state through quantum back-action [21] as well as lead to the appearance of competing higher-order nonlinear phenomena. In fact, in a recent theoretical work [22], the higher order nonlinear mixing of the electromagnetic radiation studied with the local probing laser field has been proposed in combination with homodyne detection as an alternative method for quantum noise distribution measurements with efficient background suppression.

In this work, we will present the experimental results of electro-optic field correlation measurement obtained using highly confined probing laser beams with a strong spatial overlap. Our results present a significant deviation from the expected electro-optic field correlation caused by second order nonlinear mixing of the probe pulses with the thermally populated photons in the THz regime studied in our previous works [18, 19]. We will prove that the unexpected field correlation observed arises from a third-order nonlinear mixing of the probe pulses with the electromagnetic vacuum at their own near-infrared frequency, therefore reporting, for the first time to our knowledge, the experimental verification of a nonlinear electric-field correlation on the electromagnetic vacuum due to the higher order nonlinearity term $\chi^{(3)}$.

In order to validate our hypothesis, the dependence of the detected field correlation measurement on the experimental parameters will be investigated and the parameters range in which third-order nonlinear phenomena become predominant with respect to more conventionally defined electro-optic detection will be specified. Our novel findings provide therefore a first experimental verification of the relevant parameter space in which a previously not hypothesized form of measurement back-action on electro-optic correlation, namely vacuum-assisted third-order nonlinear field correlation, can occur.

The paper is organized as follows. In section 2, we investigate both theoretically and experimentally the effect of the third-order non-linearity caused by a small NIR electric field component polarized perpendicular to the original probe polarization onto the balanced detection scheme by modulating one beam and detecting its influence on the copropagating one. In the third section, we investigate how the NIR vacuum fluctuations polarized perpendicular to the coherent probe introduce the same nonlinear mixing process and lead to a correlation in the electro-optic detection of the two probe beams. We also show that the signal arises only from the physical overlap of the two probing beams, a feature that is exploited in the non-local measurements of vacuum fluctuations.

2. Third order nonlinear balanced detection

Before analyzing the influence of higher-order nonlinearity onto the field correlation measurements of quantum states of light, we first reduce the complexity to a coherent measuring scheme. Two mutually delayed near-infrared fs-laser pulses are overlapped in a ⟨110⟩-cut zinc telluride (ZnTe) crystal as it is also the case within the correlation measurement. Then we investigate both—theoretically and experimentally—how a third-order nonlinear mixing between the two probe pulses could introduce an additional signal in the typical electro-optic detection scheme on one of the two beams.

Within the commonly used one-beam electro-optic sampling scheme, one linearly polarized fs-probe beam is overlapped with a THz-field within a nonlinear crystal. The second-order nonlinear interaction of the probe and THz field introduces an additional near-infrared field perpendicular to the original probe polarization (see figure 1). The interaction can be also understood in terms of a birefringence of the nonlinear crystal induced by the THz field. The following balanced ellipsometric measurement analyses the

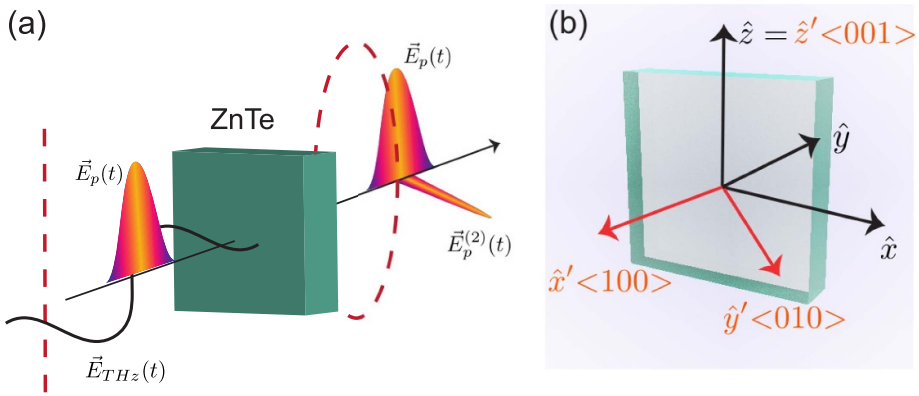

Figure 1. Balanced ellipsometry detection. (a) Electro-optic detection in ZnTe is determined by the change in polarization (red dashed line) of a femtosecond probe pulse $\vec{E}_{\mathrm{p}}(t)$ due to its second order nonlinear interaction with a phase matched THz electric field $\vec{E}_{\mathrm{THz}}(t)$ (solid black line). (b) Relative orientation of the laboratory axis (in black) and ZnTe crystallographic axis (in orange) with respect to the facet of the crystal.

change in polarization of the probe signal, which is proportional to the instantaneous electric field of the THz-radiation temporarily overlapping with the sampling probe.

For the ellipsometric analysis of the probe beam a quarter-wave plate is followed by a polarizing beam splitter. The difference in optical power between the two polarization components is measured using a differential detector. The rotation of the quarter-wave plate is chosen to have zero differential signal in the absence of any additional field generated in the nonlinear crystal. The described arrangement can be understood in the fashion of a homodyne detection. The use combination of a quarter-wave plate mixes the z-polarized probe field acting as a local oscillator with the x-polarized field generated in the nonlinear crystal. The difference in photons S detected on the two diodes of the differential detector is then proportional to the electric field E_x spectrally overlapping with the initial probe signal:

$$S = \frac{1}{2} cn\epsilon_0 \int_0^\infty \mathrm{d}\omega \frac{\eta(\omega)}{\hbar\omega} \int \mathrm{d}^2 \vec{r_\perp} |E_{p,z}(\vec{r}_\perp, \omega)|^2 \left[i \frac{E_x(\vec{r}_\perp, \omega)}{E_{p,z}(\vec{r}_\perp, \omega)} + \mathrm{h.c.} \right], \tag{1}$$

where c describes the vacuum speed of light, n the refractive index of ZnTe at NIR frequencies, ω the angular frequency and $\eta(\omega)$ the quantum efficiency of the used detector at this angular frequency and $\vec{r}_\perp$ the spatial position on the transverse plane of the probe beam.

The typical electro-optic detection process measuring THz radiation relies on sum and difference frequency generation [10]. The nonlinear interaction of a single mode ω within the broadband femtosecond probe spectrum with the THz electromagnetic mode at a much lower frequency Ω leads to the creation of modes $\omega \pm \Omega$. As long as the generated second-order electric field $E^{(2)}$ is spectrally overlapping with the probe signal, it will introduce a differential signal $S^{(2)}$. The obtained electro-optic signal depending on the time-delay τ between the THz field E_{THz} and the probe pulse can be expressed as:

$$S^{(2)}(\tau) = C \int \mathrm{d}\Omega \, R(\Omega) \, E_{\mathrm{THz}}(\Omega) \, e^{-i\Omega\tau}. \tag{2}$$

In summary, the electro-optic signal on the balanced detector is proportional to the measured THz field E_{THz} spectrally filtered by the response function $R(\Omega)$. The latter is mainly depending the absorption and phase-matching within the detection crystal and on the spectral properties of the probe signal. Using standard commercial laser sources generating a pulse duration in the order of 100 fs allows the detection in the range of a few THz, while specialized lasers with pulses of only a few fs can reach frequencies up into the mid-infrared range (MIR).

From equation (1) it can be deduced that any additionally generated field spectrally overlapping with and polarized perpendicular to the original probe field introduces a signal on the balanced detector. Significant third-order non-linearities have been observed in ZnTe crystals using tightly focused pulsed near-infrared radiation [23]. Using a pump-probe detection scheme involving two mutually delayed ultrashort pulses, it has been experimentally shown that a four-wave mixing process between a high-intensity pump and a weaker probe electric fields can lead to the generation of a signal detectable via balanced ellipsometry. For probing pulses with a temporal extent in the order of 100 fs, Gaussian beam waist smaller than 100 μm and

average optical powers in the order of tens of mW, third-order nonlinear interaction has been demonstrated to produce a probe polarization change comparable in magnitude with the one induced via electro-optic detection of THz radiation [24, 25]. Therefore, also for our experimental arrangement, the measured signal can be expected to be caused not only by second-order mixing but also to present a contribution from the third-order nonlinearity of ZnTe:

$$S = S^{(2)} + S^{(3)}. \tag{3}$$

2.1. Classical description of third order nonlinear balanced signal

In the following, the predicted influence of the third-order nonlinearity within our particular experimental configuration will be presented and we will follow the derivations reported in [24, 26]. We assume the use of two ultrashort probing pulses, mutually delayed by a time τ and both polarized along the $\hat{z}$ direction of the laboratory reference axis (figure 1). According to the tensor describing the third-order nonlinearity of ZnTe (see supplementary material), a nonlinear field along the x-axis can only be introduced in the presence of a incoming non-vanishing field along the x-axis. We will therefore assume the presence of a non-zero probe electric field component along the $\hat{x}$ axis for the initial pulse (t pulse): $\vec{E}_t(t) = (E_{t,x}(t), 0, E_{t,z}(t))$, while the delayed pulse is purely $\hat{z}$-polarized: $\vec{E}_\tau(t+\tau) = (0, 0, E_{\tau,z}(t+\tau))$. For simplicity, we will focus our analysis only on the dependence of the nonlinear signal detected by the time-delayed pulse ($t+\tau$ pulse) due to its third-order nonlinear interaction with its non-delayed version (t pulse).

According to the crystallographic symmetry of ZnTe [24], the higher-order nonlinear interaction between the two ultrashort probes will result in the creation of the following third-order polarization term along the laboratory x-axis (for further details see section I of the supplementary material):

$$P_x^{(3)}(t+\tau) = 2\epsilon_0 \chi_{44} E_{t,z}(t)\, E_{t,x}(t)\, E_{\tau,z}(t+\tau). \tag{4}$$

Here, ϵ_0 represents the vacuum permittivity and the term $\chi_{44} = 1.5 \times 10^{-19} \frac{\mathrm{m}^2}{\mathrm{V}^2}$ is the relevant component of the third-order nonlinear tensor in ZnTe [24]. Since the field polarized along the x-axis is much weaker than the field components along z, only the polarization term linear in $E_{t,x}$ is taken into account in equation (4). Furthermore the created nonlinear field $E^{(3)}$ is only copropagating with the delayed pulse for a mixing between $E_{t,z}$ and E_τ due to phase-matching. Polarization terms proportional to $E_{t,z}^2 E_{t,x}$ and $E_{\tau,z}^2 E_{t,x}$ are copropagating with the non-delayed pulse and therefore not reaching the balanced detector.

Following the steps presented in [26] in the case of classical fields, the third-order nonlinear field $E_x^{(3)}$ can be derived and inserted into equation (1). Assuming for the two interacting ultrashort probes a Gaussian distribution both in space and in the frequency domain (see supplementary material section I for details), the expression in equation (1) can be simplified as follows:

$$S_\tau^{(3)}(\tau) = \frac{\chi_{44}\omega_\mathrm{p} N_\tau \tilde{E}_{t,x}\tilde{E}_{t,z}}{ncw_0^2} \int_{-\infty}^{+\infty}\int_{-\infty}^{+\infty} \mathrm{d}\omega'\, \mathrm{d}\omega''\, \Gamma(\omega', \omega'')\, A_\mathrm{overlap}. \tag{5}$$

Here, ω_p represents the central frequency of the ultrashort probing pulse and w_0 its Gaussian waist. The amplitude at focus of the electric fields' components of the non-time delayed probe along the $\hat{x}$, $\hat{z}$ direction is indicated as $\tilde{E}_{t,x}$, $\tilde{E}_{t,z}$ respectively. The quantity N_τ represents the total number of photons in the temporal delayed pulse impinging on the balanced detector. The function A_overlap describes the spatial overlap of the two ultrashort probe pulses propagating along the nonlinear material (see supplementary material section I equation (19)). The function $\Gamma(\omega', \omega'')$ indicates the convolution of the spectral distributions of the electric fields involved in the nonlinear mixing and effectively represents the spectral intensity autocorrelation function of the two pulses.

As predicted in [24], equation (5) indicates the possible presence of a higher order nonlinear balanced signal $S^{(3)}(\tau)$ due to the interaction of two ultrashort probing pulses polarized along the $\hat{z}$ axis in ZnTe. As it is characteristic for third-order nonlinear phenomena, the amplitude of the signal generated results directly proportional to the product of the two electric field components $\tilde{E}_{t,x}, \tilde{E}_{t,z}$ (and therefore to the overall intensity) of the femtosecond pulse. This dependence also clarifies the direct connection between the arising of the higher order nonlinear balanced signal $S^{(3)}(\tau)$ and the presence of a non-vanishing component of the t probing pulse along the $\hat{x}$ direction. Moreover, the mutual interaction of the two laser probes leads to the generation of a signal $S^{(3)}(\tau)$ which represents in the time domain their intensity autocorrelation function, as derived in equation (16) of section I in the supplementary material.

2.2. Experimental verification of third order nonlinear balanced signal

In order to verify the presence of the third order induced balanced detection signal $S^{(3)}(\tau)$ predicted in equation (5) we have implemented the experimental setup sketched in figure 2(a). The setup is similar to the

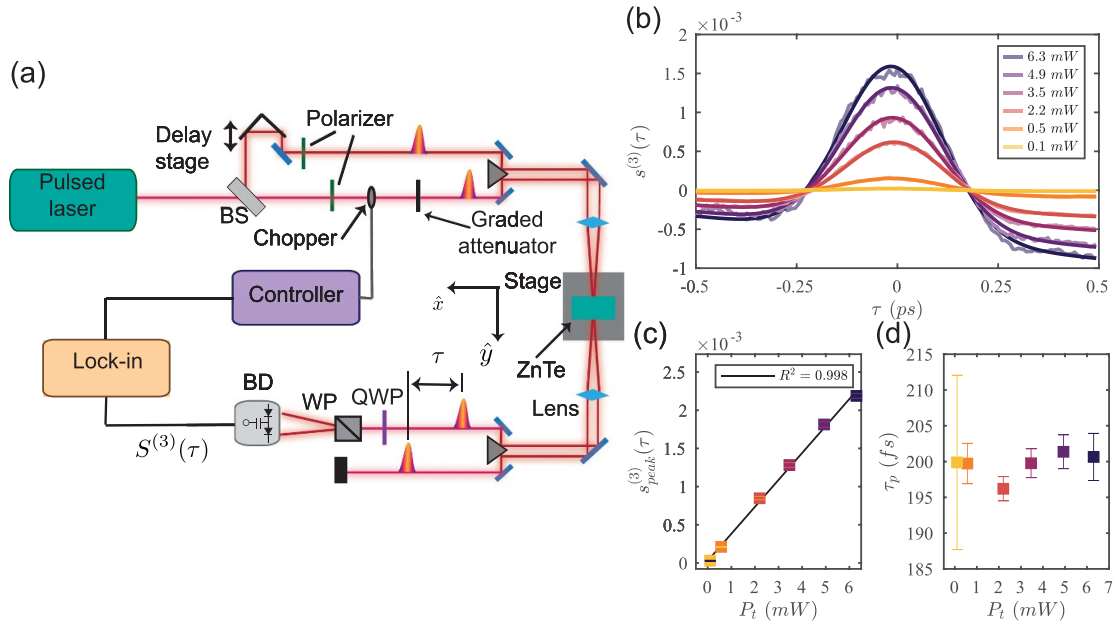

Figure 2. Third order balanced coherent detection. (a) Experimental setup used for coherent nonlinear signal detection via balanced ellipsometry. Both t and $t+\tau$ probes are polarized along the $\langle 001 \rangle$ axis of the ZnTe crystal, which coincides with the z-axis of the laboratory reference frame. The acquisition of the signal has been performed with a lock-in at the optical chopping frequency of $f = 600$ Hz. BD = balanced detectors, WP = Wollaston prism, QWP = quarter waveplate. (b) Normalized experimental third-order balanced signal $s^{(3)}(\tau)$ (faded line) recorded for different probing power of the interacting pulse P_t and their respective Gaussian fitting functions (solid lines). The experimental timetraces have been recorded with a temporal resolution of 33 fs and an integration time of 2 s per point. (c) The peak amplitude of the experimental signal $s^{(3)}_{\text{peak}}(\tau)$ presents a linear dependence with the power P_t of the copropagating interacting pulse. The uncertainty on the experimental measurement is derived from the uncertainty of the fitting parameters. (d) The extracted temporal full-width half maximum τ_p of the two interfering femtosecond pulses is retrieved from the Gaussian fitting function $g(\tau)$. The uncertainty on the reported value represents the 2σ confidence interval and it has been obtained from the uncertainty of the fitting parameters.

one reported in [25]. The ultrashort pulsed radiation generated by a Ti:Sapphire laser at a wavelength of 800 nm is divided into two equal optical paths. A delay stage on one of these paths allows an adjustable temporal delay τ between the two identical femtosecond pulses. They are subsequently collected by a system of short focal-length lenses and focused with a Gaussian beam waist of $w_0 = 10$ μm in the 1 mm long ZnTe crystal placed at the center of the lens system. The influence of the third-order nonlinear interaction between the femtosecond probes can be investigated by acquiring the balanced ellipsometry signal registered by the time delayed $t+\tau$ probe $S^{(3)}(\tau)$ via a lock-in acquisition system. No external source at THz frequencies is present and the generation of THz electromagnetic radiation via optical rectification is inhibited by the choice of the probes polarization direction along the $\hat{z}$ laboratory reference axis. The two femtosecond probes present as well a residual electric field component along the $\hat{x}$ laboratory axis, due to the non-perfect extinction ratio of the polarizers. The polarization components of the two probes present values of $P_{t,z} = 6.3$ mW, $P_{\tau,z} = 7.2$ mW and $P_{t,x} = 170$ μW, $P_{\tau,x} = 120$ μW at the detection crystal facet along the $\hat{z}$, $\hat{x}$ axis of the laboratory reference frame respectively.

While in the context of electro-optic sampling the electric field strength of the THz radiation is usually retrieved by dividing the obtained signal S with the constant $C = \frac{r_{41} n^3 l \omega_p N}{c}$, this type of normalization does not give a physical value for the signal introduced by third order nonlinear mixing. To still compare experimental data independent of the used probe power, the overall signal S has been normalized by the total number of detected photons N, which gives the relative change of the differential current in the detector $s^{(3)} = \frac{S^{(3)}}{N}$.

The experimentally obtained normalized balanced signal $s^{(3)}(\tau)$ recorded as a function of the pulses temporal delay τ is presented for different powers of the copropagating t probing pulse P_t in figure 2(b). All experimental results have been collected maintaining the optical power of the detection $t+\tau$ pulse constant. As it can be clearly observed in figure 2(b), the amplitude of the nonlinear signal $s^{(3)}(\tau)$ appears to decrease significantly as a function of the t probe power P_t. In order to obtain a more accurate estimation of the $s^{(3)}(\tau)$ amplitude dependence, the experimental data in figure 2(b) have been fitted with a Gaussian function of the form $g(\tau) = c + a\tau + b\exp(-\frac{4\ln(2)(\tau-d)^2}{\gamma^2})$. As clearly shown in figure 2(c), the peak amplitude of the fitted signal $s^{(3)}_{\text{peak}}(\tau)$ with respect to the baseline $a\tau$ presents a direct proportionality to the intensity of the

interacting probing pulse P_t, decreasing from a value of 2.2×10^{-3} for $P_t = 6.3$ mW to a value of 3×10^{-5} in the case of $P_t = 0.1$ mW. This experimental result is in good accord with the intensity dependence of a signal generated via third-order nonlinear interaction, as reported in equation (5).

As proposed in [24] and derived in equation (5), the experimental data reported in figure 2(b) should also correspond in the temporal domain to the intensity autocorrelation of the two interacting pulses $\langle I(t)I(t+\tau)\rangle$. From the fitting parameter γ, the temporal extent of the two ultrashort NIR probes can be extracted through the relation $\tau_p = 0.7\gamma$ [27]. The results obtained from the experimental data reported in figure 2(b) are presented in figure 2(d). For all the t pulse power values, the estimated temporal extent of the pulses τ_p results constant and equal to $\tau_p = 200$ fs. The result is in good agreement with the estimated value of the temporal extent of the femtosecond pulses τ_p employed in our experiment (for further information on the experimental value estimation see Note D of supplementary material in [19]).

3. Nonlinear electric field correlation of quantum electromagnetic radiation

Before discussing the influence of third-order nonlinear processes on the detection of quantum states of light, we will briefly introduce how electro-optical sampling is used to perform field correlation measurements on these states. According to the study of Moskalenko *et al* [26] the spectral electric field $E_{\mathrm{THz}}(\Omega)$ can be replaced by its operator $\hat{E}_x(\Omega)$ in equation (2). The resulting electro-optic signal operator $\hat{S}^{(2)}$ is proportional to the electric field operator $\hat{E}_x(\Omega)$ filtered by a frequency-dependent responsivity function $R(\Omega)$. Furthermore, the presence of vacuum field fluctuations at any frequency, polarization and propagation direction must be also taken into account. As a result, a NIR vacuum state of both polarization directions is copropagating with the probe beam. While any field fluctuations along z-polarization are eliminated within the balanced detection scheme, x-polarized vacuum fluctuations spectrally overlapping with the probe signal will introduce a fluctuating signal in the balanced detector $\hat{S}_n$ (see equation (1)). This noise term describes the well-known shot-noise of a photodetector in the balanced detection scheme, which is the fundamental noise limit of electro-optic sampling [11, 12, 26].

In addition, the data acquisition method differs significantly between coherent radiation measurement, as in classical THz time-domain spectroscopy, and the detection of quantum states, such as vacuum fluctuations. Coherent THz or MIR fields with a fixed phase relation to the probe pulse electric field allow for the averaging of the signal detected by many subsequent pulses. During the averaging process, shot noise is reduced and the expectation value of the measured signal operator is obtained. For incoherent quantum states, such as the ground state of light or thermal states, the expectation value of the electric field operator vanishes. Instead, the presence of those fluctuating fields manifests in the finite variance of the operator, which can be accessed by acquiring the signal for each individual pulse. Using few-fs pulses to access the MIR frequency range, it has been shown that the variance for the electro-optic signal measuring the ground state of light exceeds the shot-noise level due to the interaction with the vacuum fluctuations [11].

Furthermore, by the use of two individual probe pulses the electric field of the investigated quantum state can be accessed in two different points in space and time. The correlation of the two signals can be related to the field correlation $G^{(1)}$ of the particular state. Besides the additional information about the temporal and spatial coherence, the expectation value of the field correlation is non-zero, while the shot-noise of the two detectors is uncorrelated. Consequently the signal-over-noise ratio improves under averaging, which is crucial to be sensitive to the significantly weaker vacuum fluctuations in the lower frequency range of THz.

Figure 3(a) schematically presents how the correlation between two electro-optic signal operators $\hat{S}_t^{(2)}$ and $\hat{S}_\tau^{(2)}$ is induced by the presence of vacuum fluctuations in the THz regime. Both signals interact with the same vacuum state at two different points in time and space. The second-order fields $\hat{E}_{t,x}^{(2)}$ and $\hat{E}_{\tau,x}^{(2)}$ contain information about the THz vacuum field and are measured in homodyne detection. The corresponding signal operators are both proportional to the THz field operator and, as a result, are correlated with each other.

At the same time, we must carefully consider any other factor that may contribute to the two signals and potentially introduce a correlation. The imbalance on the differential detector can also be caused by thermal drifts in the optical setup S_{drift} or other coherent mixing processes S_{coh} as the third-order nonlinearity described in section 2, which have to be added to the overall signal:

$$\hat{S} = S_{\mathrm{drift}} + S_{\mathrm{coh.}} + \hat{S}^{(2)} + \hat{S}_n + \ldots \tag{6}$$

In particular, thermal drifts and coherent mixing between the two laser pulses alter the signal on both beams similarly, resulting in additional correlation. To eliminate those unwanted contributions to the obtained signals, we utilize a technique called 'RF-referencing'. The measurement of each of the sampling pulses is

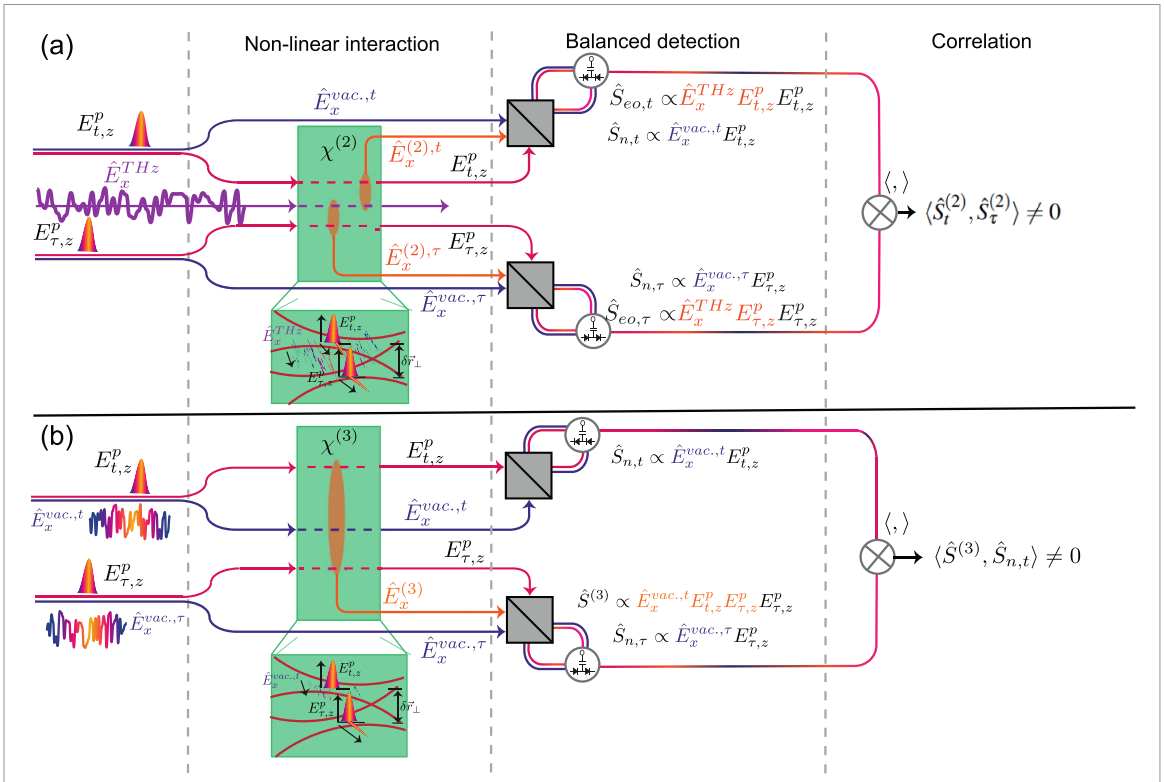

Figure 3. Comparison between correlations induced by second-order nonlinear mixing with the THz vacuum state (a) and by a third-order nonlinear mixing with the NIR vacuum field (b). (a): Both probe-fields $E^{p}_{t,z}$ and $E^{p}_{\tau,z}$ polarized along the z-axis interact individually with the same x-polarized vacuum field in the THz regime $\hat{E}^{\mathrm{THz}}_{x}$ in a second-order nonlinear mixing process. The created nonlinear fields $E^{(2),t}_{x}$ and $E^{(2),\tau}_{x}$ are co-propagating with their respective probe pulses to the balanced detection scheme, where the z-polarized field acts as a local oscillator to measure the x-polarized nonlinear field. The electro-optic signals on both detectors are proportional to the THz vacuum field and therefore a non-vanishing correlation $G^{(1)}(\tau,\delta\vec{r}_{\perp}) \propto \langle \hat{S}^{(2)}_{t} \cdot \hat{S}^{(2)}_{\tau} \rangle$ between the two signals can be observed. (b) Due to the third-order nonlinear susceptibility of ZnTe, the two electric probe fields $\vec{E}^{\mathrm{p}}_{t,z}$ and $\vec{E}^{\mathrm{p}}_{\tau,z}$ can mix with the perpendicularly polarized NIR vacuum field co-propagating with one of the two probe signals, e.g. the non-delayed beam $\hat{E}^{\mathrm{vac.},t}_{x}$. The k-vector of the generated nonlinear electric field $\hat{E}^{(3)}_{x}$ is determined by the phase-matching and parallel to the other probe field, in this case the delayed signal $\vec{E}^{\mathrm{p}}_{\tau,z}$. In the homodyne mixing between those two fields, a signal $S^{(3)}$ proportional to the causing NIR vacuum field. The very same vacuum field is mixing on the other homodyne detection line with $\vec{E}^{\mathrm{p}}_{t,z}$ causing the shot-noise and leading to a non-vanishing correlation between the two signals.

referred to their respective temporal adjacent pulse. They are described by the operators $\hat{S}(t+T_{\mathrm{rep}},\vec{r})$ and $\hat{S}(t+\tau+T_{\mathrm{rep}},\vec{r}+\delta\vec{r}_{\perp})$ respectively. Here the quantity T_{rep} represents the time occurring between each couple of measurement pulses. As described in the Methods section of [18], the measured correlation function will be given by the expression:

$$\left\langle \left(\hat{S}(t)-\hat{S}\left(t+T_{\mathrm{rep}}\right)\right)\left(\hat{S}(t+\tau)-\hat{S}\left(t+\tau+T_{\mathrm{rep}}\right)\right)\right\rangle . \tag{7}$$

This specific measurement configuration will allow the efficient suppression of systematic coherent noise affecting each individual pulse equally, such as higher-order nonlinear balanced signal $S^{(3)}(\tau)$ described in section 2.2, and long time drifts, such as $1/f$-noise. Therefore, it confers to the nonlinear field correlation measurement technique sensitivity only to radiation presents with a coherence time smaller than T_{rep} by design. Assuming no further influences on the imbalance signal $\hat{S}$ than in equation (6), the measured correlation using RF-referencing will be dominated by the correlation between the two electro-optic signals caused by the THz vacuum fluctuations. Consequently, it is proportional to the first-order field correlation function of the investigated vacuum state within the detection bandwidth:

$$G^{(1)}(\tau;\vec{r}_1,\vec{r}_2)=\left\langle\left\{\hat{E}(t,\vec{r}_1),\hat{E}(t+\tau,\vec{r}_2)\right\}\right\rangle \propto \left\langle\left\{\hat{S}^{(2)}(t,\vec{r}_1),\hat{S}^{(2)}(t+\tau,\vec{r}_2)\right\}\right\rangle . \tag{8}$$

$\{,\}$ indicates the anti-commutator of the two operators and $\langle\ \rangle$ the quantum mechanics expectation value applied to the investigated quantum state of light. Since the two beams can be moved individually inside the crystal in arbitrary positions $\vec{r}_1$ and $\vec{r}_2$, the first order correlation function $G^{(1)}(\tau;\vec{r}_1,\vec{r}_2)$ can be investigated both in space and time [18, 19].

The discussion so far considers the third-order nonlinear mixing process only in the presence of a coherent x-polarized NIR field. The agreement of experimental correlation measurements on the ground state of light and theoretical predictions of $G^{(1)}$ supports this assumption. At the same time, vacuum fluctuations in the NIR are copropagating with the probe signal and its x-polarized component is causing the shot-noise on the balanced detectors. As depicted in figure 3(b) the very same vacuum state can introduce an additional incoherent signal $\hat{S}^{(3)}$ on the other probe signal via third-order nonlinear mixing, which is then correlated to the shot-noise of the initial pulse. Due to the incoherent nature of the causing vacuum fluctuations, RF-referencing cannot remove this type of signal and it can affect the measurement of $G^{(1)}(\tau)$, especially when using tightly focused beams, which are overlapping temporally and spatially inside the nonlinear crystal.

In the following subsection, we derive the correlation between this incoherent third-order nonlinear signal and the shot-noise on the detector of the other probe signal. Afterward, we demonstrate that in a similar experiment as shown in [18] but using tightly focused beams, the measured correlation will deviate strongly from the expected behavior of $G^{(1)}$. The further investigation of the observed correlation depending on different experimental parameters in section 3.3 agrees well with the theoretical predictions for the mentioned higher order correlation introduced by a third-order nonlinear mixing process.

3.1. Quantum description of third-order nonlinear correlation of electromagnetic radiation

For simplicity, we will consider the influence of the electromagnetic vacuum $\hat{E}_x^{\mathrm{vac.},t}$ copropagating with the non-time delayed t probe $E_{t,z}^{\mathrm{p}}(t)$ on the quantum balanced ellipsometry signal detected by the time delayed $t+\tau$ probing pulse $E_{\tau,z}^{\mathrm{p}}(t+\tau)$. Both probes are polarized along the $\hat{z}$ axis of the laboratory reference frame, as indicated in the pedices notation. The symmetric process obtained by exchanging the roles of time-delayed and not time-delayed probes can be shown to be formally equivalent.

According to second quantization formalism, the amplitude of the electromagnetic vacuum at NIR frequency can be described as $\hat{E}^{\mathrm{vac}} = i\sum_k \sqrt{\frac{\hbar\omega_k}{2\epsilon_0 n^2 V}}\left[\hat{a}_k e^{-i\omega_k t+i\vec{k}\cdot\vec{r}} - \hat{a}_k^{\dagger} e^{i\omega_k t-i\vec{k}\cdot\vec{r}}\right]$. Here the quantum operator $\hat{a}^{(\dagger)}$ describes the destruction (creation) of a NIR mode of frequency ω_k propagating with wavevector $\vec{k}$ inside the nonlinear material. In analogy with equation (4), the third-order nonlinear polarization arising due to the interaction of the quantum electromagnetic vacuum with the high-intensity classical electric field of the two probes can be written as:

$$\hat{P}_x^{(3)}(t+\tau) = 2\epsilon_0\chi_{44}E_{t,z}^{\mathrm{p}}(t)\,E_{\tau,z}^{\mathrm{p}}(t+\tau)\,\hat{E}_x^{\mathrm{vac.},t}. \tag{9}$$

The term $\hat{P}_x^{(3)}(t+\tau)$ reported in equation (9) serves as a source term for the generation of the additional polarization component of the temporal delayed $t+\tau$ laser pulse $\hat{E}^{(3)}(t+\tau)$, as indicated in figure 3. The latter induces the balanced nonlinear signal at the photodetector described via the quantum mechanic operator $\hat{S}^{(3)}(t+\tau,\delta\vec{r}_\perp)$. It can be expressed as (for detailed derivation, see section II A of supplementary material):

$$\begin{aligned}\hat{S}^{(3)}(t+\tau,\vec{r}+\delta\vec{r}_\perp) &= \frac{1}{2}cn\epsilon_0\int_0^{+\infty}\mathrm{d}\omega\,\frac{\eta(\omega)}{\hbar\omega}\int d^2\vec{r}_\perp|E_{\tau,z}^{\mathrm{p}}(\zeta)|^2\left[i\,\frac{\hat{E}^{(3)}}{E_{\tau,z}^{\mathrm{p}}(\zeta)}+\mathrm{h.c.}\right]\\ &= -\frac{2\chi_{44}E_t^{\mathrm{p}}N_\tau\omega_c}{3cn}\int\mathrm{d}^2\vec{r}_\perp g_0^2\left(\vec{r}-\frac{\delta\vec{r}_\perp}{2}\right)g_0\left(\vec{r}+\frac{\delta\vec{r}_\perp}{2}\right)\sum_{\tilde{k}}\sqrt{\frac{\hbar\omega_{\tilde{k}}}{2\epsilon_0\epsilon_r V}}\\ &\quad\times\left[\hat{a}_{\tilde{k}}e^{-i\omega_{\tilde{k}}t+i\vec{\tilde{k}}\cdot\delta\vec{r}_\perp}R\left(\tilde{k}_y,\omega_{\tilde{k}}\right)-\mathrm{h.c.}\right].\end{aligned} \tag{10}$$

Here the functions $g_0(\vec{r}\pm\frac{\delta\vec{r}_\perp}{2})$ represent the Gaussian spatial distribution of the two probing pulses centered symmetrically at $\pm\frac{\delta\vec{r}_\perp}{2}$ with respect to the origin of the laboratory reference frame (at the crystal center). N_τ indicates the number of photons of the $t+\tau$ probe effectively measured at the photodetector. The function $R(\tilde{k}_y,\omega_{\tilde{k}})$ represents the responsivity of the third-order nonlinear interaction, which is dependent on the phase matching condition of the near-infrared modes with component $\tilde{k}_y$ along the pulses propagation direction and frequency $\omega_{\tilde{k}}$. $R(\tilde{k}_y,\omega_{\tilde{k}})$ is only non-vanishing for the propagation direction $\tilde{k}_y$ parallel to the propagation of the not delayed probe field E_τ and for frequencies $\omega_{\tilde{k}}$ within the NIR spectral range. Any other k-vector is not supported by phase-matching and frequencies outside the region of the NIR probe spectrum do not create a third-order nonlinear field overlapping spectrally with the probe field.

The quantum vacuum at near-infrared frequencies $\hat{E}_x^{\mathrm{vac.},t}$ is responsible for the generation of shot noise associated with its photodetection, as also appearing directly in [26]. The measurement of the latter is described through the quantum mechanics operator $\hat{S}_{n,t}$:

$$\begin{aligned}\hat{S}_{n,t(\tau)} &= \frac{1}{2}cn\epsilon_0\int_0^{+\infty}\mathrm{d}\omega\frac{\eta(\omega)}{\hbar\omega}\int\mathrm{d}^2\vec{r}_\perp\left[\left(E^{\mathrm{p}}_{t(\tau),z}(\zeta)\right)^* i\hat{E}_x^{\mathrm{vac.},t(\tau)}+\mathrm{h.c.}\right]\\ &= -\frac{N_t\omega_c}{E^{\mathrm{p}}_{t,z}}\sum_{\tilde{k}'}\sqrt{\frac{\hbar\omega_{\tilde{k}'}}{2\epsilon_0\epsilon_r V}}\left[\hat{a}_{\tilde{k}'}e^{-i\omega_{\tilde{k}'}t+i\tilde{k}'_x O_t^i}-\mathrm{h.c.}\right]f(\omega_{\tilde{k}'})\,\Gamma\left(\tilde{k}'_x,\tilde{k}'_z\right).\end{aligned} \tag{11}$$

The functions $f(\omega_{\tilde{k}'})$ and $\Gamma(\tilde{k}'_x,\tilde{k}'_z)$ indicate the detection responsivity for a single electromagnetic quantum vacuum mode characterized by frequency $\omega_{\tilde{k}'}$ and transverse wavevectors components $\tilde{k}'_x,\tilde{k}'_z$ respectively. An equivalent expression can be derived for the shot noise operator $\hat{S}_{n,\tau}$ of the delayed $t+\tau$ probe.

Following the derivations present in literature, the quantum mechanics operator $\hat{S}$ describing the complete result of the balanced ellipsometry measurement performed by the two femtosecond pulses in the space-time points $(t,\vec{r}),(t+\tau,\vec{r}+\delta\vec{r}_\perp)$ individually can be written as a sum of the following contributions:

$$\hat{S}_{\mathrm{t}}(t,\vec{r}) = \hat{S}^{(2)}(t,\vec{r})+\hat{S}^{(3)}(t,\vec{r})+\hat{S}_{n,t}, \tag{12a}$$

$$\hat{S}_{\tau}(t+\tau,\vec{r}+\delta\vec{r}_\perp) = \hat{S}^{(2)}(t+\tau,\vec{r}+\delta\vec{r}_\perp)+\hat{S}^{(3)}(t+\tau,\vec{r}+\delta\vec{r}_\perp)+\hat{S}_{n,\tau}. \tag{12b}$$

Here the operators $\hat{S}^{(2)}(t,\vec{r})$, $\hat{S}^{(2)}(t+\tau,\vec{r}+\delta\vec{r}_\perp)$ are related to the electro-optic measurement of THz electromagnetic radiation, as defined in [18]. Rewriting equation (7) as a function of the quantum operators defined in equation (12*a*) and equation (12*b*), the final experimental result will be given by the expectation value of the quantum operator on a thermally populated radiation state. Taking into consideration only the lower nonlinear contribution terms, the result will read:

$$\begin{aligned}\left\langle\left\{\hat{S}_{\mathrm{t}}(t,\vec{r}),\hat{S}_{\tau}(t+\tau,\vec{r}+\delta\vec{r}_\perp\right\}\right\rangle &= \left\langle\left\{\hat{S}^{(2)}(t,\vec{r}),\hat{S}^{(2)}(t+\tau,\vec{r}+\delta\vec{r}_\perp)\right\}\right\rangle+\left\langle\left\{\hat{S}^{(3)}(t,\vec{r}),\hat{S}_{n,\tau}\right\}\right\rangle\\ &\quad+\left\langle\left\{\hat{S}^{(3)}(t+\tau,\vec{r}+\delta\vec{r}_\perp),\hat{S}_{n,t}\right\}\right\rangle.\end{aligned} \tag{13}$$

Here, $\{,\}$ indicates the anti-commutator of the two operators and $\langle\,\rangle$ the quantum mechanics expectation value on a quantum thermal state of radiation, which can be formally described as a statistical mixture state. According to quantum mechanics, the only non-vanishing terms upon computation of the expectation value of equation (13) will be terms presenting both the normally ordered $\hat{a}^\dagger\hat{a}$ and not normally ordered $\hat{a}\hat{a}^\dagger$ creation and destruction operators relative to the same electromagnetic mode. The first surviving term $\left\langle\left\{\hat{S}^{(2)}(t,\vec{r}),\hat{S}^{(2)}(t+\tau,\vec{r}+\delta\vec{r}_\perp)\right\}\right\rangle$ represents the electro-optic electric field correlation $G^{(1)}(\tau,\delta\vec{r}_\perp)$ of THz electromagnetic radiation, as defined in [18, 19]. The additional terms $\left\langle\left\{\hat{S}^{(3)}(t,\vec{r}),\hat{S}_{n,\tau}\right\}\right\rangle$ and $\left\langle\left\{\hat{S}^{(3)}(t+\tau,\vec{r}+\delta\vec{r}_\perp),\hat{S}_{n,t}\right\}\right\rangle$ are induced from the correlation of the electromagnetic vacuum responsible for the shot noise characterizing one ultrashort probe with the third order nonlinear balanced signal induced by the same quantum vacuum on the copropagating pulse. Due to wave-vector conservation, the nonlinear balanced signal detected individually by each femtosecond pulse could not arise from a four-wave mixing process induced via its own quantum vacuum. It is also important to note that the same argument cannot be applied to the quantum vacuum fluctuations at THz frequencies, due to their very long wavelength that relaxes the phase-matching condition.

The shot noise in the two photodetectors also results uncorrelated $\langle\{\hat{S}_{n,t},\hat{S}_{n,\tau}\}\rangle = 0$, as discussed in the chapter introduction.

To summarize, a simple quantum mechanical description of both the noise characterizing the two probes and of the incoherent nonlinear balanced ellipsometry measurement predicts, in addition to the term arising from the THz quantum thermal radiation, the existence of two additional correlation terms $\left\langle\left\{\hat{S}^{(3)}(t,\vec{r}),\hat{S}_{n,\tau}\right\}\right\rangle+\left\langle\left\{\hat{S}^{(3)}(t+\tau,\vec{r}+\delta\vec{r}_\perp),\hat{S}_{n,t}\right\}\right\rangle$ arising from a third-order mixing between the quantum vacuum at the NIR frequency and the propagating pulse of the other line. In other words, vacuum fluctuations responsible for the shot noise on one line mix with the pulse on the other line and create a correlated noise affecting the latter after the ellipsometry measurement.

3.2. Experimental verification of nonlinear field correlation

The investigation of quantum field correlation measurement on the thermally populated electromagnetic state has been carried out using the experimental setup reported in figure 4(a). The system is similar to the

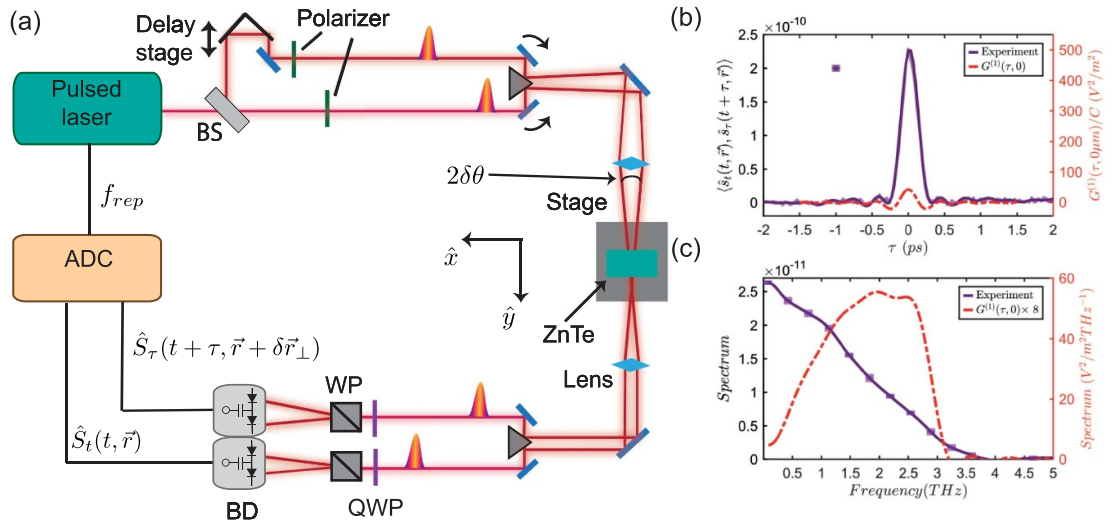

Figure 4. Experimental quantum higher order nonlinear correlation. (a) The experimental setup for nonlinear electric field correlation measurements allows the control of both the temporal and spatial distance between probes. The latter is controlled via a couple of piezo mirrors, which confer a relative propagation angle of $2\delta\theta$ to the two probes. The acquisition of the experimental measurement points is performed at the repetition rate of the femtosecond laser $f_{\text{rep}} = 80$ MHz. BD = Balanced detectors, WP = Wollaston prism, QWP = Quarter waveplate. (b) and (c) Experimental electric field correlation measurement results performed with a beams' spatial separation of $\delta\vec{r} = 0$ μm in time (b) and frequency domain (c) (in faded purple). For better visualization, the data have been filtered with a Kaiser windowing function (in solid purple). For comparison, the numerically simulated result for the electro-optic field correlation $G^{(1)}(\tau, \delta\vec{r}_\perp = 0)$ of THz thermal radiation at 300 K is reported in dashed-dotted lines. In both figures, the experimental uncertainty indicates the 2σ confidence interval.

one presented in figure 2(a), but in addition to the temporal distance between the two probing ultrashort pulses, also their spatial distance $\delta\vec{r}_\perp$ in the transverse plane can be controlled via a symmetric couple of piezo mirrors. The change in the propagation angle $\delta\theta$ with respect to the femtosecond pulses propagation direction $\hat{y}$ will be translated by the lens system into a spatial separation $\delta\vec{r}_\perp = f\delta\theta$. The two femtosecond probing pulses are focused by the lens onto the detection crystal, where they will sample the same electromagnetic state at two different space-time points. Afterward, they will be individually analyzed via balanced ellipsometry, where the acquisition is performed at the repetition rate of the laser $f_{\text{rep.}}$. The recording of the results obtained from each couple of near-infrared pulses allows the real-time computation of the electric field correlation function as described in equation (7).

The experimental nonlinear field correlation measurement obtained using the setup presented in figure 4(a) with overlapping sampling beams of Gaussian beam waist $w_0 = 10$ μm, temporal extent $\tau_{\text{p}} = 200$ fs and peak electric field amplitude of $E_z^{\text{p}} = 10$ MV/m are reported in figures 4(b) and (c) in time and frequency domain respectively. As shown in figure, the results measured using the specified set of experimental parameters for perfectly overlapping sampling beams $\delta\vec{r}_\perp = 0$ differ significantly both in amplitude and most importantly in spectral content from the expected electro-optic THz field correlation $G^{(1)}(\tau, |\delta\vec{r}_\perp| = 0)$ generated via blackbody emission from the environment at 300 K, also shown for comparison. The latter has been numerically estimated using the expression reported in equation (2) of [18] and the experimental parameters of the femtosecond probing pulses employed in the experiment.

The experimental field correlations have been filtered with a Kaiser windowing function, in order to reduce the presence of noise-induced artefacts (for more information see supplementary Note 3 of [19]). Similarly to the data in section 2, the experimental results are normalized with the total number of detected photons of the respective detector N_t and N_τ, so we obtain the correlation between the relative signals:

$$\langle \hat{s}_t(t,\vec{r}) \cdot \hat{s}_\tau(t+\tau,\vec{r}+\delta\vec{r}_\perp)\rangle = \frac{\langle \hat{S}_t(t,\vec{r}) \cdot \hat{S}_\tau(t+\tau,\vec{r}+\delta\vec{r}_\perp)\rangle}{N_t \cdot N_\tau}. \tag{14}$$

To compare the data to previous measurements [18, 19] of the electro-optic field correlation $G^{(1)}(\tau,\delta\vec{r})$ a second scale converting the correlation of the relative signal to the corresponding field correlation in $\text{V}^2\,\text{m}^{-2}$ has been added on the right side of the plots.

As reported in figure 4(b), the amplitude of the experimental signal presents a peak-to-peak amplitude of around $\langle \hat{s}_t(t) \cdot \hat{s}_\tau(t+\tau)\rangle_{\text{pp}} = 2.3 \times 10^{-10}$, which results approximately ten times larger than the expected correlation of THz photons $\langle \hat{s}_t^{(2)}(t) \cdot \hat{s}_\tau^{(2)}(t+\tau)\rangle_{\text{pp}} = 2.5 \times 10^{-11}$. The two curves present significant

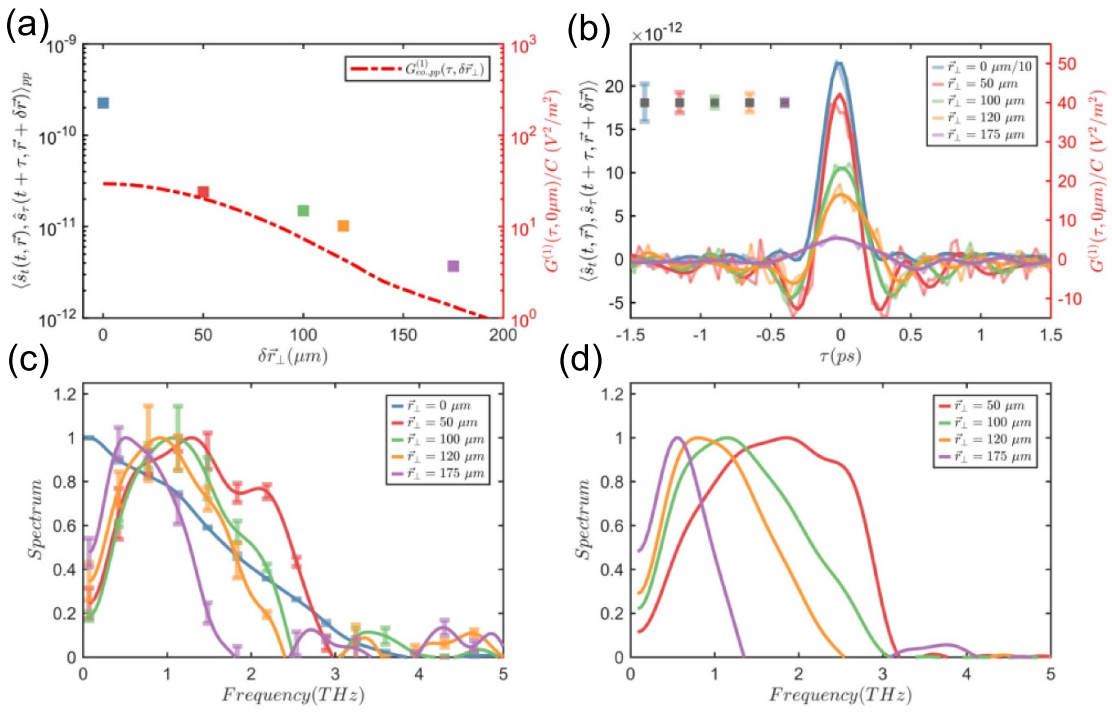

Figure 5. Quantum higher order nonlinear correlations as a function of beam separation. (a) Dependence of the peak-to-peak amplitude measured relative correlation $\langle \hat{s}_t(t,\vec{r}) \cdot \hat{s}_\tau(t+\tau,\vec{r}+\delta\vec{r}_\perp)\rangle_{\rm pp}$ (in log scale) as a function of the transverse beam separation $\delta\vec{r}_\perp$. For comparison, also the peak-to-peak amplitude of the electro-optic field correlation of THz modes $\langle \hat{s}^{(2)}(t,\vec{r}) \cdot \hat{s}^{(2)}(t+\tau,\vec{r}+\delta\vec{r}_\perp)\rangle$ is reported (dash-dotted line). (b) and (c) Experimental nonlinear correlation measurements in time (b) and frequency domain (c) for increasing $\delta\vec{r}_\perp$. All errorbars represent the 2σ confidence interval. (d) Numerically computed electro-optic electric field correlation $\langle \hat{s}^{(2)}(t,\vec{r}) \cdot \hat{s}^{(2)}(t+\tau,\vec{r}+\delta\vec{r}_\perp)\rangle$ at $T = 300$ K for spatial beams separation $\delta\vec{r}_\perp$ reported in (b) and (c) for non-overlapping beams.

differences as well in frequency content, as shown by their Fourier transformation in figure 4(c). The spectral content of the numerically simulated electric field correlation $G^{(1)}(\tau, 0\ \mu\text{m})$ depends on the spectral properties of the black body radiation within the bandwidth of the electro-optic detection and therefore presents mostly contributions from higher frequency components around 2 THz. On the contrary, the experimental spectrum derived from figure 4(b) presents maximum contributions in the low-frequency components regions with a maximum centered at zero frequency, where there field strength of black body radiation and vacuum fluctuations vanishes.

3.3. Experimental study of nonlinear field correlation depending on experimental parameters

The nature of the measured nonlinear correlation has been investigated by studying its dependence on experimental parameters such as temperature, crystal length, and probing pulses' wavelength, power, and spatial distance $\delta\vec{r}_\perp$. In order to compare the nonlinear correlation measurement to the numerically predicted results induced by electro-optic detection of thermal THz radiation $G^{(1)}(\tau,\delta\vec{r}_\perp)$, the experimental measurements presented in this section have also been normalized by the electro-optic correlation constant C and reported in a scale of $\text{V}^2\ \text{m}^{-2}$ as defined in section 3.

As derived theoretically in section III A and more in detail in section II A of the supplementary material, the higher-order nonlinear correlation term $\left\langle \left\{ \hat{S}^{(3)}(t+\tau,\vec{r}+\delta\vec{r}_\perp), \hat{S}_{n,t} \right\} \right\rangle$ and the THz blackbody induced field correlation $G^{(1)}(\tau,\delta\vec{r}_\perp)$ will present strongly different temporal coherence characteristics, which will strongly depend on the sampling beams transverse separation $\delta\vec{r}_\perp$. This dependence has been investigated experimentally. The measured nonlinear correlation $\langle \hat{s}_t(t,\vec{r}) \cdot \hat{s}_\tau(t+\tau,\vec{r}+\delta\vec{r}_\perp)\rangle$ amplitude dependence on the relative distance between the sampling probes $\delta\vec{r}_\perp$ is reported both in time and frequency domain in figure 5.

In figure 5(a) the total peak-to-peak amplitude of the measured nonlinear correlation $\langle \hat{s}_t(t,\vec{r}) \cdot \hat{s}_\tau(t+\tau,\vec{r}+\delta\vec{r}_\perp)\rangle_{\rm pp}$ is reported as a function of the relative transverse distance between the sampling probes $\delta\vec{r}_\perp$. As the latter increases, the nonlinear correlation significantly decreases in amplitude from a value of $\langle \hat{s}_t(t,\vec{r}) \cdot \hat{s}_\tau(t+\tau,\vec{r}+\delta\vec{r}_\perp)\rangle_{\rm pp} = 2.3 \times 10^{-10}$ in the case of perfectly overlapping sampling beams $|\delta\vec{r}_\perp| = 0\ \mu$m to a value of $\langle \hat{s}_t(t,\vec{r}) \cdot \hat{s}_\tau(t+\tau,\vec{r}+\delta\vec{r}_\perp)\rangle_{\rm pp} = 3.7 \times 10^{-12}$ for a transverse beam separation of

$|\delta\vec{r}_\perp| = 175\ \mu$m. As shown in figure by comparison with the numerically simulated result, for spatially overlapping sampling laser probes the measured correlation is dominated by higher-order nonlinear terms $\langle \hat{s}_{\mathrm{n},t} \cdot \hat{s}^{(3)}_\tau(t+\tau, \vec{r}+\delta\vec{r}_\perp)\rangle + \langle \hat{s}^{(3)}_t(t,\vec{r}) \cdot \hat{s}_{\mathrm{n},\tau}\rangle$, while for sampling beams with a spatial transverse distance equal several times their diameters the experimental results are well predicted by the electro-optic field correlation of THz thermal radiation $G^{(1)}(\tau, \delta\vec{r}_\perp)$. A similar behavior can be observed also employing different nonlinear ZnTe detection crystals of various lengths, as shown in section III in the supplementary material.

As expected, the experimental correlation measurements performed for different probing beams' distances present significant differences not only in amplitude but in the extent of their temporal coherence as well, as it is reported in figure 5(b). The experimental result measured in the case of $|\delta\vec{r}_\perp| = 0\ \mu$m preserves its temporal coherence for a time of 0.5 ps. An increase in spatial distance between sampling probes $\delta\vec{r}_\perp$ correlates on the other hand with an increased temporal extent of the nonlinear correlation, which is preserved for over 2 ps for all the measurements. This difference is reflected in the spectral content of the sampled broadband radiation in the case of overlapping and non-overlapping sampling pulses, which are reported in figure 5(c). As it can be seen in figure, the spectral content of the nonlinear correlation measured with $|\delta\vec{r}_\perp| = 0\ \mu$m presents a large bandwidth of 3.5 THz with the majority of the contributions given by lower frequency modes around 0 THz, in good agreement with a major contribution stemming from the higher-order nonlinear correlation $\langle \hat{s}_{\mathrm{n},t} \cdot \hat{s}^{(3)}_\tau(t+\tau, \vec{r}+\delta\vec{r}_\perp)\rangle + \langle \hat{s}^{(3)}_t(t,\vec{r}) \cdot \hat{s}_{\mathrm{n},\tau}\rangle$. On the other hand, the experimental result obtained with the sampling beams non-overlapping inside the nonlinear material $|\delta\vec{r}_\perp| > 50\ \mu$m show low spectral contributions from the low-frequency region. Moreover, their spectral contents present a varying bandwidth and peak contribution frequency, which decrease from a value of 3 THz and 1.5 THz respectively for the measurement performed with $|\delta\vec{r}_\perp| = 50\ \mu$m to values of 1.75 THz and 0.75 THz for the nonlinear correlation measured with $|\delta\vec{r}_\perp| = 175\ \mu$m. The decrease in bandwidth as well as the redshift of the peak contribution frequency for nonlinear correlation measured with non-spatially overlapping probes ($|\delta\vec{r}_\perp| > 50\ \mu$m) presents a good agreement with the numerical results for electro-optic field correlation of thermal THz radiation, reported in figure 5(d). As it is shown in figure, the numerical THz electro-optic correlation estimated for different transverse beams spatial separations $\delta\vec{r}_\perp$ present almost identical bandwidths to the experimental results and similar redshift in the peak contribution frequency, which decrease from a value of 3.2 THz and 2 THz respectively for the measurement performed with $|\delta\vec{r}_\perp| = 50\ \mu$m to values of 1.4 THz and 0.6 THz for the nonlinear correlation measured with $|\delta\vec{r}_\perp| = 175\ \mu$m. The redshift of the peak contribution frequency of the THz electro-optic correlation can be intuitively explained in the spatial domain with electromagnetic modes of wavelength equal or smaller than twice the spatial transverse distance between the sampling pulses providing negative or null contributions to the measured field correlation.

In order to corroborate the hypothesis on the origin of the higher-order nonlinear correlation from a vacuum-assisted four-wave mixing of the overlapping probing pulses, a further analysis of its dependence on the experimental parameters has been performed. The experimental results obtained as a function of different crystals, environment temperature and probes' power and wavelength are reported in figure 6. All the measurements shown have been performed with perfectly overlapping sampling beams $|\delta\vec{r}_\perp| = 0\ \mu$m.

The higher-order nonlinear correlation measurements obtained employing different lengths of the $\langle 110\rangle$-cut ZnTe detection crystal are reported in figure 6(a). As it can be seen, the normalized nonlinear correlation measurement performed using two distinct 1 mm long and a 2 mm long ZnTe detection crystals are all characterized by the presence of a higher order correlation term, whose amplitude increases from a peak value of $\langle \hat{s}_t(t,\vec{r}) \cdot \hat{s}_\tau(t+\tau,\vec{r})\rangle = 1.1 \times 10^{-10}$ for the 1 mm long crystal to a value of $\langle \hat{s}_t(t,\vec{r}) \cdot \hat{s}_\tau(t+\tau,\vec{r})\rangle = 1.4 \times 10^{-10}$ for the 2 mm long crystal due to the increased interaction length. All the measurements present however similar temporal coherence, which is preserved for a period of 0.75 ps. Their common origin in both crystals is further highlighted by their comparison in frequency domain, presented in figure 6(b). All experimental measurements present exactly the same spectral content, with a bandwidth of around 2 THz and the majority of the contributions originating from the lower frequency region around 0 THz. The latter is in good agreement with a nonlinear correlation signal generated via third-order nonlinear mixing of the probes mediated via the electromagnetic vacuum, as described in equation (33) of supplementary material in section II A.

A further indication of the third-order nonlinear origin of the measured signal is shown in figure 6(c), where the measurements performed employing a sampling pulses probing powers of $P_t = P_\tau = 1.6$ mW and $P_t = P_\tau = 0.8$ mW respectively are shown. Given the power normalization introduced in equation (14), the experimental higher-order nonlinear correlation measurements appear to be directly proportional to the product of the power of the sampling probes P_t, P_τ. This result is once more in good agreement with the expected power dependency of a third-order induced nonlinear correlation, as shown in equation (33) of supplementary material in section II A.

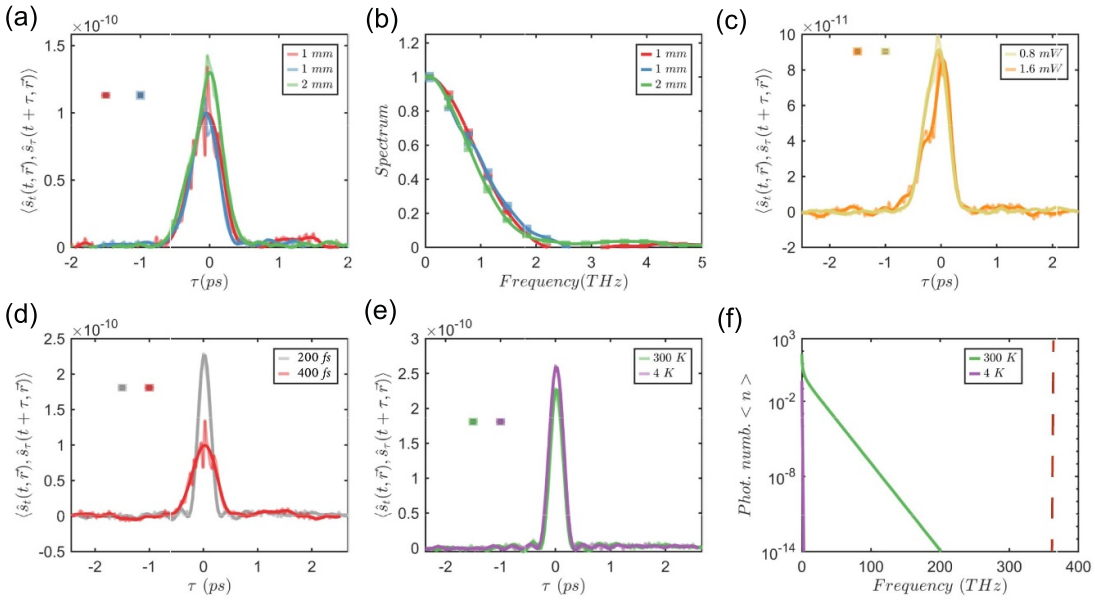

Figure 6. Experimental parameters dependence. (a) and (b) Higher order nonlinear correlation measurement in time (a) and frequency domain (b) employing two different 1 mm and a 2 mm long ⟨110⟩-cut ZnTe detection crystal. The experimental parameters used are: $P_t = P_\tau = 0.8$ mW, $\tau_p \approx 400$ fs, $\lambda = 780$ nm. (c) Third-order nonlinear correlation measurement for different sampling laser pulses' power. Both measurements have been performed using a 1 mm long ZnTe crystal, $\tau_p \approx 400$ fs and $\lambda = 780$ nm. (d). Experimental nonlinear correlation measured utilizing pulses with a temporal duration of $\tau_p = 200$ fs ($\lambda = 800$ nm) and $\tau_p \approx 400$ fs ($\lambda = 780$ nm). The measurements have been performed using the same ⟨110⟩-cut ZnTe crystal. (e) Effect of the temperature of the blackbody radiation detected on the higher order nonlinear correlation $\langle \hat{s}_t(t,\vec{r}) \cdot \hat{s}_\tau(t+\tau,\vec{r}) \rangle$. (f) Average number of photons per mode $\langle n \rangle$ according to Planck's radiation law at different temperatures of 300 K (orange) and 4 K (yellow). The central frequency of the ultrashort probing pulse employed in the experiment $\omega_c = 375$ THz is reported in blue dashed line. The errorbars in all the experimental measurements in figure represent the 2σ confidence interval.

The dependence of the balanced ellipsometry correlation amplitude on the pulse-length of the sampling probe pulses τ_p is reported in figure 6(d). As it can be seen in figure, the use of shorter pulses $\tau_p = 200$ fs leads to a higher order nonlinear correlation of peak-to-peak amplitude of around $\langle \hat{s}_t(t,\vec{r}) \cdot \hat{s}_\tau(t+\tau,\vec{r}) \rangle = 2.3 \times 10^{-10}$, twice as large with respect to the result obtained using 400-fs-pulses due to the higher peak power. The change in pulse length becomes also visible in the temporal extent of the observed correlation signal, which increases with the pulse length.

The influence of the temperature T of the thermal radiation to which the ZnTe detection crystal is exposed and, as a consequence, of the average number of photons per mode $\langle n \rangle$ populating the incoherent quantum radiation responsible for the nonlinear correlation is reported in figure 6(e). As shown in figure, the change in temperature T of the blackbody radiation measured does not affect significantly the amplitude of the higher order nonlinear correlation amplitude, which increases from a peak-to-peak value of $\langle \hat{s}_t(t,\vec{r}) \cdot \hat{s}_\tau(t+\tau,\vec{r}) \rangle = 2.3 \times 10^{-10}$ at $T = 300$ K to a value of $\langle \hat{s}_t(t,\vec{r}) \cdot \hat{s}_\tau(t+\tau,\vec{r}) \rangle = 2.5 \times 10^{-10}$ at $T = 4$ K. The experimental result is in good agreement with a higher-order correlation term generated via the electromagnetic vacuum at NIR frequencies. As it can be seen in figure 6(f), the average number of photons per mode $\langle n \rangle$ at NIR frequencies, given by Planck's radiation law, in the frequency range around the central frequency of the infrared probing pulse $\omega_c = 375$ THz remains below a value of $\langle n \rangle < 10^{-14}$ for both temperatures.

4. Conclusion

In this work, we have shown how third-order nonlinearity at NIR frequencies can affect the balanced ellipsometry measurement performed with ZnTe, both on the signal measured by the individual pulses and most importantly on their correlation.

In section 2.1 we have derived theoretically the properties in time and in frequency domain of the third-order coherent signal induced on each of the sampling pulses due to their mutual interaction in the nonlinear material. The predictions have been corroborated by the experimental results reported in section 2.2.

In a balanced field correlation measurement, third-order nonlinearities have also been shown to play a significant role in the generation of correlation between the incoherent signals measured by the two sampling pulses. As proven theoretically in section 3.1, the electromagnetic vacuum at NIR frequencies characterizing the noise of one pulse can interact with the copropagating one inside the nonlinear medium, leading to the change of its polarization. Upon measurement, the vacuum-induced change in polarization of one femtosecond pulse will therefore result correlated with the noise of the copropagating pulse, which is induced by the same quantum vacuum. Consequently, the described correlation relies on the non-trivial fact, the well-known shot-noise in a photo-detector is caused by the vacuum-fluctuations in the detected spectral region.

The experimental characterization of the vacuum-assisted third-order nonlinear correlation has been reported in section 3.3. Here, the analysis of the spatial nonlinear correlation of incoherent radiation clearly indicates the presence of two different regimes. Whilst for spatially overlapping sampling beams the nonlinear correlation result is dominated by the four-wave mixing due to the quantum vacuum at NIR frequencies, for increasing distance between the sampling pulses the experimental results return to a good agreement with electro-optic field correlation of THz thermal radiation.

A detailed analysis of the experimental parameters dependence of the third-order nonlinear correlation further verifies its connection to the electromagnetic vacuum at NIR frequencies, given its independence on temperature, power dependence and its presence with similar features in different crystals. All our experimental findings present a good agreement with the predicted measurement parameters dependence of the responsivity of the higher-order nonlinear correlation, derived in section II A and B of the supplementary material. The qualitative analysis of the latter, moreover, clearly implies the significant contributions of the described correlations vanishes for correlation measurements less tightly focused beams as have been used in [18] or not overlapping focal spots [19].

Because two-beam correlation experiments, in contrast to single-beam studies [11, 12], allow the identification of the frequency components contributing to the correlation signal, they also have allowed to isolate the contribution from the higher order non-linear signal that is inevitably mixed into the electro-optic sampling of the THz radiation. Furthermore, it shows that measuring two nearby spatial locations with beams that do not physically overlap is a very efficient strategy to remove such contribution while increasing the detection sensitivity and allowing further studies of the quantum vacuum [19].

Data availability statement

The data that support the findings of this study will be openly available following an embargo at the following URL/DOI: http://hdl.handle.net/20.500.11850/632247.

Acknowledgments

The experimental work was funded by the Swiss National Science Foundation (Grant No. 200020 192330/1) and the National Centre of Competence in Research Quantum Science and Technology (NCCR QSIT) (Grant 51NF40-185902) (F F S, A H). We acknowledge the mechanical workshop at ETHZ. We acknowledge the contributions of Dr Cristina Ileana Benea-Chelmus for their contributions to previous work, Dr E Mavrona for the extraction of the refractive index of ZnTe. We thank Prof. Denis Seletskiy for fruitful discussion.

Conflict of interest

The authors declare no conflict of interest.

Authors contribution

J F and F F S conceived the idea for the experiment and its theoretical interpretation. F F S and A H conducted the measurements. The data analysis was primarily performed by F F S and their results were interpreted by F F S, A H and J F. The theoretical framework was developed by F F S. J F was the scientific supervisor of this work. The manuscript was written through contributions from all authors. All authors have given approval to the final version of the manuscript.

ORCID iDs

Francesca Fabiana Settembrini https://orcid.org/0000-0002-2017-4695
Alexa Herter https://orcid.org/0000-0003-0370-8736
Jérôme Faist https://orcid.org/0000-0003-4429-7988

References

[1] Chang D E, Vuletić V and Lukin M D 2014 *Nat. Photon.* **8** 685
[2] Kimble H J 2008 *Nature* **453** 1023
[3] Knill E, Laflamme R and Milburn G J 2001 *Nature* **409** 46
[4] Schlawin F 2017 *J. Phys. B: At. Mol. Opt. Phys.* **50** 203001
[5] Giovannetti V, Lloyd S and Maccone L 2011 *Nat. Photon.* **5** 222
[6] Miller D A B 2010 *Nat. Photon.* **4** 3
[7] Uppu R *et al* 2020 *Sci. Adv.* **6** eabc8268
[8] Luo K-H, Brauner S, Eigner C, Sharapova P R, Ricken R, Meier T, Herrmann H and Silberhorn C 2019 *Sci. Adv.* **5** eaat1451
[9] Pirandola S, Bardhan B R, Gehring T, Weedbrook C and Lloyd S 2018 *Nat. Photon.* **12** 724
[10] Gallot G and Grischkowsky D 1999 *J. Opt. Soc. Am.* B **16** 1204
[11] Riek C, Seletskiy D V, Moskalenko A S, Schmidt J F, Krauspe P, Eckart S, Eggert S, Burkard G and Leitenstorfer A 2015 *Science* **350** 420
[12] Riek C, Sulzer P, Seeger M, Moskalenko A S, Burkard G, Seletskiy D V and Leitenstorfer A 2017 *Nature* **541** 376
[13] Kizmann M, Guedes T L d M, Seletskiy D V, Moskalenko A S, Leitenstorfer A and Burkard G 2019 *Nat. Phys.* **15** 960
[14] Guedes T L M, Kizmann M, Seletskiy D V, Leitenstorfer A, Burkard G and Moskalenko A S 2019 *Phys. Rev. Lett.* **122** 053604
[15] Sulzer P *et al* 2020 *Phys. Rev.* A **101** 033821
[16] Virally S, Cusson P and Seletskiy D V 2021 *Phys. Rev. Lett.* **127** 270504
[17] Benea-Chelmus I-C, Bonzon C, Maissen C, Scalari G, Beck M and Faist J 2016 *Phys. Rev.* A **93** 043812
[18] Benea-Chelmus I-C, Settembrini F F, Scalari G and Faist J 2019 *Nature* **568** 202
[19] Settembrini F F, Lindel F, Herter A M, Buhmann S Y and Faist J 2022 *Nat. Commun.* **13** 3383
[20] Valentini A 1991 *Phys. Lett.* A **153** 321
[21] Guedes T L M, Vakulchyk I, Seletskiy D V, Leitenstorfer A, Moskalenko A S and Burkard G 2023 *Phys. Rev. Res.* **5** 013151
[22] Gündoğdu S, Virally S, Scaglia M, Seletskiy D V and Moskalenko A S 2023 *Laser Photon. Rev.* **n/a** 2200706
[23] Chen X, He S, Shen Z, Li Zhao F, Xu K Y, Wang G, Wang R and Dai N 2009 *J. Appl. Phys.* **105** 023106
[24] Caumes J-P, Videau L, Rouyer C and Freysz E 2002 *Phys. Rev. Lett.* **89** 047401
[25] Tian Z, Wang C, Xing Q, Gu J, Li Y, He M, Chai L, Wang Q and Zhang W 2008 *Appl. Phys. Lett.* **92** 041106
[26] Moskalenko A S, Riek C, Seletskiy D V, Burkard G and Leitenstorfer A 2015 *Phys. Rev. Lett.* **115** 263601
[27] Siegman A E 1986 *Lasers* (University Science Books)